

REPORT DOCUMENTATION PAGE

Form Approved
OMB NO. 0704-0188

Public Reporting burden for this collection of information is estimated to average 1 hour per response, including the time for reviewing instructions, searching existing data sources, gathering and maintaining the data needed, and completing and reviewing the collection of information. Send comment regarding this burden estimates or any other aspect of this collection of information, including suggestions for reducing this burden, to Washington Headquarters Services, Directorate for Information Operations and Reports, 1215 Jefferson Davis Highway, Suite 1204, Arlington, VA 22202-4302, and to the Office of Management and Budget, Paperwork Reduction Project (0704-0188), Washington, DC 20503.

1. AGENCY USE ONLY (Leave Blank)

2. REPORT DATE 02/21/2005

3. REPORT TYPE AND DATES COVERED
FINAL - 6/1/2004 to 2/28/2005

4. TITLE AND SUBTITLE

Wing Force & Moment Characterization of Flapping Wings for Micro Air Vehicle Application

5. FUNDING NUMBERS

C: W911NF-04-1-0110

6. AUTHOR(S)

Zaeem A. Khan and Sunil Sunil K. Agrawal

7. PERFORMING ORGANIZATION NAME(S) AND ADDRESS(ES)

University of Delaware
Newark, DE 19716

8. PERFORMING ORGANIZATION
REPORT NUMBER

9. SPONSORING / MONITORING AGENCY NAME(S) AND ADDRESS(ES)

U. S. Army Research Office
P.O. Box 12211
Research Triangle Park, NC 27709-2211

10. SPONSORING / MONITORING
AGENCY REPORT NUMBER

46897.1-EG-II

11. SUPPLEMENTARY NOTES

The views, opinions and/or findings contained in this report are those of the author(s) and should not be construed as an official Department of the Army position, policy or decision, unless so designated by other documentation.

12 a. DISTRIBUTION / AVAILABILITY STATEMENT

Approved for public release; distribution unlimited.

12 b. DISTRIBUTION CODE

13. ABSTRACT (Maximum 200 words)

This paper presents a general method for investigating the unsteady aerodynamics of flapping wings for micro air vehicle application. For this purpose, a dynamically scaled robotic flapper was designed and fabricated which can flap the wings in a desired kinematic pattern. A quasi-steady aerodynamic model and wing testing methodology was developed based on unsteady aerodynamic mechanisms. This model additionally accounts for the wing twisting. The experimental results show a good agreement with published data. 24 kinematic patterns were tested and the quasi-steady aerodynamic model compares well with the experimental results. The focus of the present work is on hovering flight, however, the methodology is general and can be extended to slow forward flight in future.

14. SUBJECT TERMS

15. NUMBER OF PAGES

18

16. PRICE CODE

17. SECURITY CLASSIFICATION
OR REPORT
UNCLASSIFIED

18. SECURITY CLASSIFICATION
ON THIS PAGE
UNCLASSIFIED

19. SECURITY CLASSIFICATION
OF ABSTRACT
UNCLASSIFIED

20. LIMITATION OF ABSTRACT
UL

Wing Force and Moment Characterization of Flapping Wings for Micro Air Vehicle Application

Zaeem A. Khan, Graduate Student, Sunil K. Agrawal, Ph.D., Professor

Department of Mechanical Engineering
University of Delaware, Newark, DE 19716
agrawal@me.udel.edu

Abstract— This paper presents a general method for investigating the unsteady aerodynamics of flapping wings for micro air vehicle application. For this purpose, a dynamically scaled robotic flapper was designed and fabricated which can flap the wings in a desired kinematic pattern. A quasi-steady aerodynamic model and wing testing methodology was developed based on unsteady aerodynamic mechanisms. This model additionally accounts for the wing twisting. The experimental results show a good agreement with published data. 24 kinematic patterns were tested and the quasi-steady aerodynamic model compares well with the experimental results. The focus of the present work is on hovering flight, however, the methodology is general and can be extended to slow forward flight in future.

I. INTRODUCTION

The creation of flapping wing micro air vehicles (FWMAV) is a challenging problem. Flapping wing flight offers high maneuverability and the capability to hover as witnessed in insects and hummingbirds. These properties make FWMAVs more suitable for micro air vehicle missions such as reconnaissance and surveillance, specially, in confined areas. The aerodynamics of flapping wings, such as that of insects and hummingbirds, is unsteady. The flow over the wings is a function of time and this makes unsteady aerodynamics extremely complex. Unlike conventional fixed and rotary wing vehicles, the flapping wing aerodynamics is still a largely unexplored area.

As shown in Fig. 1, the aerodynamic module is fundamental to the design process of a FWMAV. The module takes the wing and body kinematics as inputs and gives the aerodynamic forces and torques. These are then used to compute the rigid body dynamics, navigation and control algorithms, and to perform design optimization.

Due to the complexity of solving Navier-Stokes equation [2] for flow around flapping wings and possible inaccuracies in the theoretical modeling, we have selected the experimental method to determine the aerodynamic forces and moments based on blade element analysis. Experimental investigation of flapping wing aerodynamics based on fruit fly (*Drosophila*) kinematics has been reported [9]. Flow visualization experiments using scaled hawkmoth wings were performed [7, 8]. These experiments led to the discovery of certain unsteady aerodynamic mechanisms that are responsible for high lift in biological flying species.

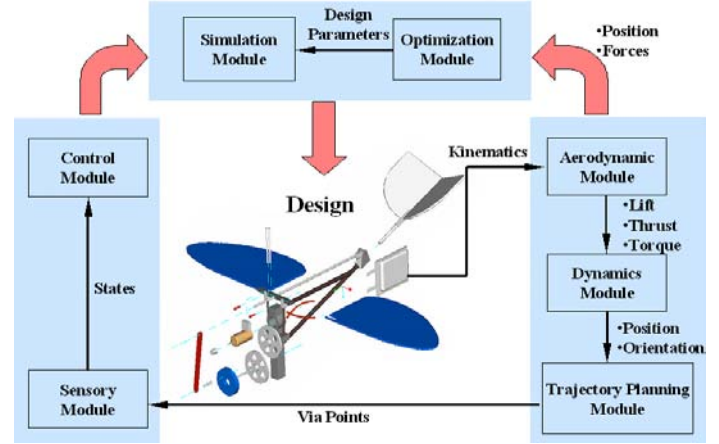


Fig. 1. The architecture of FW-MAV Design

In our work, we conduct experiments on flapping wings using a robotic flapper. However, our focus is the FWMAV aerodynamics and design. Therefore, we keep the wing kinematics to be very general and use a generic insect-like wing for testing. We have taken into account the effects of wing twist along the span, since wings of large insects and hummingbirds show marked twisting compared to small insects such as *Drosophila*. The moments and the location of force on the wing are also determined experimentally using a six-axis force torque sensor. We also present a mathematical model of flapping wing aerodynamics which constitutes the aerodynamic module.

The main goal of this paper is to present a method for determining the force coefficients to be used in the aerodynamic model. Using this methodology, the coefficients of a number of wing shapes and geometries can be catalogued analogous to NACA airfoil sections. This information can then be utilized for designing insect-like MAV's or for comparison of aerodynamic characteristics of different wing planforms.

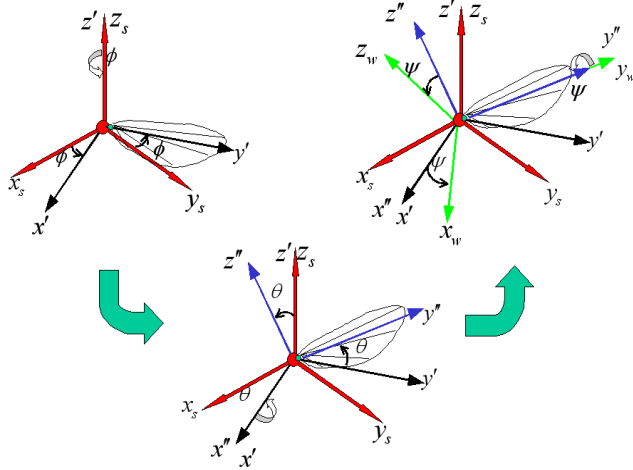
The organization of this paper is as follows: Section II describes the flapping wing kinematics. Section III presents a derivation of the aerodynamic model along with the assumptions. Section IV outlines the experimental setup. In Section V, we present a modification to the aerodynamic model based on the initial experimental data. Section VI

explains the methodology of determining the coefficients in the aerodynamic model. In Section VII, the experimental results are compared with published data and in Section VIII, we compare the quasi-steady aerodynamic model with the experimental results. Finally, conclusions are presented in Section IX.

II. KINEMATICS

A. Wing motion analysis

We consider the left wing of a typical insect. For the right wing motion, a similar but different rotation sequence is required and will not be considered here. As shown in Fig. 2, the wing frame (x_w, y_w, z_w) can be described by three successive rotations with respect to frame (x_s, y_s, z_s) attached at the wing base. First, rotation about z_s axis by an angle ϕ , next a rotation about the current x' axis by an angle θ and finally rotation about the current y'' axis by an angle ψ . Therefore, the wing position is given by the body sequence 3-1-2 rotation and by angles (ϕ, θ, ψ) . The y_w axis attached to the wing is the feather axis.



$$(x_s, y_s, z_s) \xrightarrow{(z_s; \phi)} (x', y', z') \xrightarrow{(x'; \theta)} (x'', y'', z'') \xrightarrow{(y''; \psi)} (x_w, y_w, z_w)$$

Fig. 2. Figure showing the body sequence 3-1-2 which gives the three rotation angles (ϕ, θ, ψ)

Wing angles can be represented by Fourier series given below [10]:

$$\phi(t) = \phi_o + \sum_{n=1}^{\infty} \Phi_n \sin(n\omega t + \zeta_{\phi_n}), \quad (1)$$

$$\theta(t) = \theta_o + \sum_{n=1}^{\infty} \Theta_n \sin(n\omega t + \zeta_{\theta_n}), \quad (2)$$

$$\psi(t) = \psi_o + \sum_{n=1}^{\infty} \Psi_n \sin(n\omega t + \zeta_{\psi_n}), \quad (3)$$

where ω is the flapping speed in radians/sec, Φ_n, Θ_n, Ψ_n are the flapping amplitudes and $\zeta_{\phi_n}, \zeta_{\theta_n}$ and ζ_{ψ_n} are the phase differences.

B. Terminology

Stroke plane

The plane defined by (x_s, y_s) axes represents the stroke plane as shown in Fig. 2. The frame (x_s, y_s, z_s) is referred to as the *stroke plane frame*. The motion of the feather axis is not necessarily confined to the stroke plane due to θ , the elevation or out of stroke plane angle.

Planar flapping

If the out of stroke plane angle θ is zero, the motion is called planar flapping. In this paper, we will consider planar flapping.

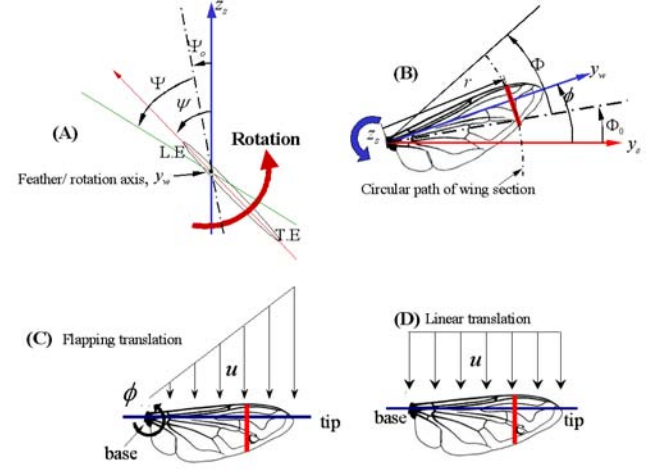


Fig. 3. Motion terminology: (A) Rotational Motion of a wing section about the feather axis given by ψ . (B) Translational motion of the section about the flapping axis given by ϕ . The difference between flapping translation and linear translation is shown in (C) and (D).

Translational motion

Linear translation [11] is the wing motion where the entire wing moves forward perpendicular to the feather axis in such a way that the velocity of the base and the tip of the wing are the same as shown in Fig. 3(D). Therefore, every section of the wing moves along a straight line path with the same velocity. A conventional aircraft wing undergoes linear translation. In flapping translation [11], the wing tip rotates around the flapping axis fixed at the base as shown in Fig. 3(C). Therefore, the velocity along the wing increases linearly from the root to the tip such that a section of the wing translates along a circular path as shown in Fig. 3(B). Insect wings undergo flapping translation. A section of helicopter rotor blade undergoes flapping translation since the section follows a circular path. However, unlike insect flapping motion, it can trace a complete circle. For a wing section located at a distance r from the flapping

axis, the translational speed $|\bar{u}_T(r, t)|$ is given by $\dot{\phi}r$ as shown in Fig 4(C) and the translational acceleration along the circular path is $\ddot{\phi}r$.

Flap amplitude

For a single frequency motion, the flap amplitude is an important parameter of the wing kinematics, denoted by Φ as shown in Fig. 3(B). The total stroke amplitude is labeled as $\bar{\Phi}$, which is twice the flap amplitude Φ . Φ_0 is the mean stroke amplitude. The *mid-stroke* is that position of the wing where $\phi = \Phi_0$ as shown in Fig. 3(B). When $\Phi_0 \neq 0$, the motion is called *asymmetric flapping*. When $\Phi_0 = 0$, the motion is referred to as *symmetric flapping*.

Rotational motion

Wing rotation refers to the rotation of the wing about the feather axis through an angle ψ as shown in Fig. 3(A) and given by Eq. (3). Flapping wing typically rotates at the extremes of the stroke. When the wing goes from upstroke to downstroke, the rotation is called *pronation*. Similarly, rotation between downstroke and upstroke is called *supination*. The rotational speed and rotational acceleration are $\dot{\psi}$ and $\ddot{\psi}$, respectively.

Rotational amplitude

The rotational amplitude is denoted by Ψ . As shown in Fig 3(A), Ψ_0 is the mean rotational amplitude. For *symmetric rotation*, $\Psi_0 = 0$, otherwise the motion is referred to as *asymmetric rotation*.

Angle of attack

The angle of attack is the angle between the chord at a location r from the wing base and the relative flow velocity $\bar{u}_T(r, t)$. Mathematically, α is given by

$$\alpha = \pm \tan^{-1}\left(\frac{u_n}{u_t}\right), \quad -\pi/2 < \alpha < \pi/2, \quad (4)$$

where u_t and u_n are the components of $\bar{u}_T(r, t)$ along the normal \hat{n} and axial \hat{t} axes fixed to the airfoil section shown in Fig. 4(B). The \pm in Eq. (4) takes the sign of u_t .

Mean angle of attack ($\bar{\alpha}$)

We define the mean angle of attack $\bar{\alpha}$ as the angle of attack of a section located at a distance $\hat{r}_2 R$ along the span and having the chord length equal to the mean chord \bar{c} [3]. \hat{r}_2 is the radius of gyration of the wing area non-dimensionalized by the wing length R [3]. Therefore, $\bar{\alpha}$ is given by Eq. (4)

$$\bar{\alpha} = \pm \arctan\left(\frac{u_n(\hat{r}_2 R, t)}{u_t(\hat{r}_2 R, t)}\right), \quad -\pi/2 < \bar{\alpha} < \pi/2 \quad (5)$$

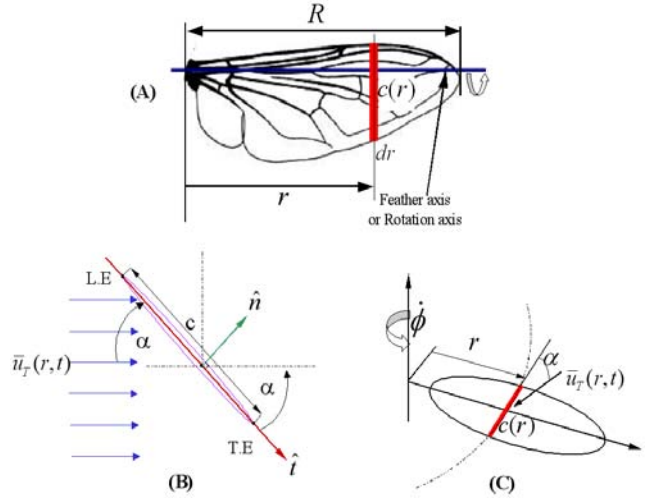


Fig. 4. (A) Wing geometry of a typical insect. (B) shows the definition of angle of attack at a wing section. (C) The angle of attack remains constant during the translational motion of a section. If translational speed $|\bar{u}_T(r, t)| = \dot{\phi}r$ is also held constant, then the flow over the section is steady-state.

III. AERODYNAMIC MODEL

A. Quasi-steady state analysis

If the flow velocity at a location on the wing does not change with respect to time, it is referred to as steady state flow. In order to maintain steady state flow over an airfoil section, it is required that the section be placed in a flow of constant velocity U_∞ and at a fixed orientation, i.e., the angle of attack α with respect to time be fixed in an inertial frame. The steady-state aerodynamic force is given by

$$F = C_F(\alpha) 1/2 \rho U_\infty^2 A. \quad (6)$$

where F is the aerodynamic force such as lift or drag, U_∞ is the relative flow velocity, A is the wing area and ρ is the air density. $C_F(\alpha)$ is the coefficient of the aerodynamic force. It is a function of the angle of attack α of the wing.

The steady state force equation for flapping wing can be derived using the blade element method (BEM). The force on a strip of wing at a distance r from the flapping axis is given by

$$dF = C_F(\alpha) 1/2 \rho |\bar{u}_T(r, t)|^2 c(r) dr, \quad (7)$$

where $C_F(\alpha)$ is the force coefficient of an element of the wing which is a function of the local angle of attack α and $c(r)dr$ is the area of the section as shown in Fig. 4(A). Eq. (7) can be integrated for the entire wing as follows

$$F = 1/2 \rho \int_0^R C_F(\alpha) |\bar{u}_T(r, t)|^2 c(r) dr, \quad (8)$$

The force coefficient can also be defined for the entire wing based on the mean angle of attack $\bar{\alpha}$. Therefore, Eq. (8) can be written as

$$F = C_F(\bar{\alpha}) 1/2 \rho \int_0^R |\bar{u}_T(r, t)|^2 c(r) dr. \quad (9)$$

In the hope of finding approximate analytical solutions to the flapping wing aerodynamics, simplified models based on quasi-steady state assumption have been developed [15]. According to quasi-steady state assumption, the motion kinematics during flapping cycle is replaced by a series of static positions having instantaneous velocity and angle of attack [3]. The force is determined using Eq. (7) or (8) which is not a function of wing rotation and acceleration. It is only a function of the translational velocity $\bar{u}_T(r, t)$ of the wing. Therefore, we refer to quasi-steady state force as the translational force. In this method, any time dependence of the aerodynamic force arises from the time dependence of the kinematics but not that of the fluid flow itself. Ellington [3] used quasi-steady analysis to investigate insect flight and determined that the analysis underestimated the lift required to support an insect during hovering and concluded that a substantial revision of the quasi-steady method is necessary. He further proposed that the quasi-steady state model must include wing rotation in addition to flapping translation.

B. Quasi-unsteady state analysis

Since Ellington's investigation [3], several researchers have provided more data to support the insufficiency of the quasi-steady model (Ennos, 1989a; Zanker and Gotz, 1990; Dudley, 1991). These developments have spurred the search for specific unsteady mechanisms and mathematical models to explain the aerodynamic forces on insect wings. Dickinson [9],[12] used experimental investigation to determine the aerodynamics of hovering fruitfly. According to Dickinson [12], the total instantaneous aerodynamic force on the wing can be represented as a sum of four force components given below;

$$F_{inst} = F_a + F_{trans} + F_{rot} + F_{wc}, \quad (10)$$

where F_{inst} is the instantaneous aerodynamic force, F_a is the force due to virtual mass effect and F_{trans} is the instantaneous translational force, F_{rot} is the rotational force and F_{wc} is the force due to wake capture. Dickinson did not provide a mathematical form for wake capture effect. However, wake capture effect was identified from the experimental data. Delaurier [1] presented a theoretical model of flapping wings based on circulation theory of lift. In Delaurier's model, the wake capture effect is also modeled in addition to rotational and virtual mass forces. Walker [13] also presented a semi-empirical model of flapping wings with an alternate mathematical form for the rotational force. Walker applied this model to the fruitfly wing and found good comparison with both the experimental results of fruitfly experiment by Dickinson et

al and the CFD-modeled forces on the virtual fruitfly wing (Sun and Tang, 2002 [16]).

Based on a study of quasi-unsteady aerodynamic models presented by Dickinson [12], Delaurier [1] and Walker [13], we modify the quasi-steady model given by Eq. (8) as follows

$$F_T = F_{steady}(\dot{\phi}) + F_{unsteady}(\dot{\phi}, \dot{\psi}, \ddot{\phi}, \ddot{\psi}), \quad (11)$$

where F_T is the total instantaneous force on the wing, F_{steady} is the steady state or translational force given by Eq. (9) and $F_{unsteady}$ is the unsteady force which is a function of wing rotation and acceleration. In this paper, we will refer to this method as quasi-unsteady since the total force F_T is implicitly dependent on time. The current focus is to determine the mathematical form of $F_{unsteady}$.

C. Unsteady effects

Leading edge vortex (LEV) Force

When a thin wing translates at a high angle of attack close to the stall, the flow breaks up at the leading edge and rolls into a leading edge vortex (LEV). The presence of this vortex increases the circulation and, thereby, the lift force significantly. In conventional airplane wings, this effect occurs momentarily before stall. However, in insects such as hawkmoths, the flapping translation motion stabilizes the vortex and it remains attached to the wing during the entire stroke [2], [7]. LEV was shown to remain attached even in rotating wings at high angles of attack [5], [6]. Therefore, based on this study, we conclude that LEV force is not a function of wing rotation and acceleration and it can be modeled by steady-state Eq. (9) which can be written as

$$F_{lev} = C_1(\bar{\alpha}) 1/2 \rho \int_0^R |\bar{u}_T(r, t)|^2 c(r) dr = C_1 F_1. \quad (12)$$

Equation (12) can be thought of as a product of a function $F_1 = 1/2 \rho \int_0^R |\bar{u}_T(r, t)|^2 c(r) dr$ which captures the physics of $F_{steady} = F_{lev}$ and a coefficient $C_1 = C_1(\bar{\alpha})$ that adjusts the magnitude. Since F_{lev} is generated during the translational phase of wing motion, it can be referred to as translational force.

Rotational Force

If the wing rotates about the feather axis with an angular rate $\dot{\psi}$, a rotational circulation force is generated [12]. In this paper, we use the mathematical form of rotational force given by Walker [13]. It says that rotational force can be modeled by selecting the flow velocity $|\bar{u}_T(r, t)|$ in Eq. (12) at a location 'i' along the chord as shown in the Fig. 5(A). The total flow velocity $\bar{u}(r, t)$ can be written as a vector sum of translational velocity $\bar{u}_T(r, t)$ and rotational velocity $\bar{u}_R(r, t)$. The magnitude of $\bar{u}_R(r, t)$ is dependent on d_o and d_i which are percentage distances along the chord $c(r)$. The parameter d_i is an unknown

constant while d_o is known from wing geometry and can vary along the span. Therefore $d_o = d_o(r)$. The coefficient of rotational force C_2 appears as the non-dimensional parameter $d_i - d_o(r)$ in the expression for $|\bar{u}(r, t)|$ which can be adjusted to scale the rotational force. Therefore,

$$C_2(r) = d_i - d_o(r). \quad (13)$$

Note that if the rotational axis lies ahead of the leading edge then $d_o(r)$ should be taken as negative. Therefore C_2 can vary along the span depending upon the wing geometry unless $d_o(r) = 0$. The combined LEV and rotational force is given as

$$F_{lev+rot} = C_1 \frac{1}{2} \rho \int_0^R |\bar{u}(r, t)|^2 c(r) dr, \quad (14)$$

where the coefficient C_2 appears in the expression for $|\bar{u}(r, t)|$. If the wing has only translation, i.e. $\dot{\psi}$ is zero, then Eq. (14) simplifies to Eq. (12) and we get the translational force only. In Fig. 5(A), note that the angle of attack α due to combined rotational and translational velocity is greater than α_T due to translational velocity alone.

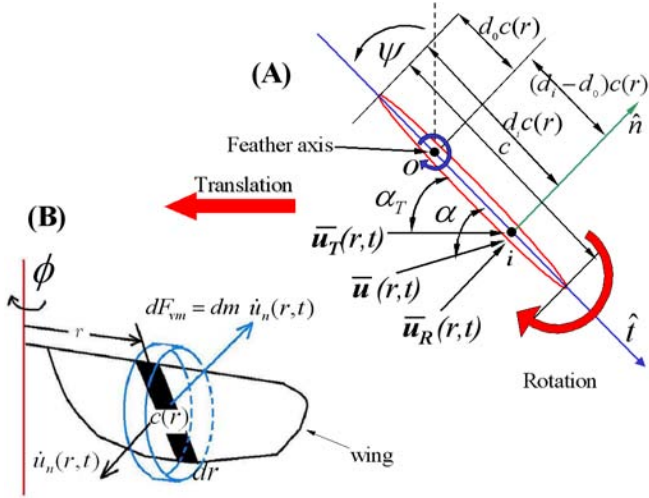


Fig. 5. (A) The combined rotational and translational/LEV effect on a wing section located at a distance 'r' from the flapping axis. $\bar{u}_T(r, t)$ is the translational velocity, $\bar{u}_R(r, t)$ is the rotational velocity and $\bar{u}(r, t)$ is the vector sum of translational and rotational velocities. (B) Virtual mass force acting at a section located at a distance 'r' from the flapping axis. Here, $\dot{u}_n(r, t)$ is the component of acceleration normal to the wing surface in the wing frame and ' dm ' is the mass of air assumed to be contained in a cylinder of diameter $c(r)$ and height dr .

Virtual Mass force

As the wing accelerates, it moves along with it a mass of air, assumed to be contained in a cylinder with diameter equal to the chord [1], [3]. The acceleration of this mass

of air shows up as a virtual mass force (see Fig. 5(B)) and can be written as

$$dF_{virtual\ mass} = dm \dot{u}_n(r, t), \quad (15)$$

where $\dot{u}_n(r, t)$ is the rate of change of normal velocity component at the mid-chord location in the wing frame and dm is the mass of air enclosed in a thin cylinder of width dr and a diameter equal to the chord c at a distance r from the flapping axis. The mass of air is $\rho\pi c^2/4$. Therefore, Eq. (15) can be written as

$$dF_{virtual\ mass} = \frac{\rho\pi}{4} \dot{u}_n(r, t) c(r)^2 dr. \quad (16)$$

On integrating Eq. (16) from root to the tip of the wing, we get the total force given by

$$F_{virtual\ mass} = C_3 \frac{\rho\pi}{4} \int_0^R \dot{u}_n(r, t) c(r)^2 dr = C_3 F_3 \quad (17)$$

The coefficient of virtual mass C_3 is included in order to adjust the magnitude while the function F_3 captures the physics of virtual mass effect.

D. Total Force

The total aerodynamic force including translational (LEV effect), rotational and virtual mass effects can be written as

$$F_T \cong C_1 \frac{\rho}{2} \int_0^R |\bar{u}(r, t)|^2 c(r) dr + C_3 \frac{\rho\pi}{4} \int_0^R \dot{u}_n(r, t) c(r)^2 dr. \quad (18)$$

Here, the LEV and rotational forces are combined as the first term in the above equation. C_1 and C_3 are the coefficients of LEV and virtual mass force respectively. The coefficient of rotational force, C_2 , appears implicitly in $\bar{u}(r, t)$.

E. Assumptions in the model

- Superposition of steady and unsteady aerodynamic effects holds.
- LEV force can be modeled by the steady-state aerodynamic equation.
- Chordwise-force due to skin friction is ignored. This is based on the results of revolving wing experiments [5],[6].
- The total force F_T acts normal to the chord throughout the flapping cycle, i.e. we assume that $C_1 F_1$, $F_2(C_1 C_2)$ and $C_3 F_3$ act normal to the chord at every section of the wing.
- The total force F_T acts at the mid-chord location at every section of the wing.

IV. EXPERIMENTAL INVESTIGATION

A. Flow similarity

In order to determine the coefficients C_1 , C_2 and C_3 in Eq. (18), we conducted experimental investigation. The basis of experimental investigation is flow similarity which ensures that the coefficients are similar for the actual and the experimental wing. In order to achieve flow similarity, the reduced frequency parameter K along with Reynolds number Re and wing geometry should match for the actual and experimental wing. The wing size, flapping speed and fluid medium can be different. Therefore,

$$C_1 = C_2 = f(Re, K, geometry) \quad (19)$$

It is shown in [17] that the virtual mass force depends on Reynolds number and wing geometry

$$C_3 = f(Re, geometry) \quad (20)$$

The flow Reynolds number Re and reduced frequency K for the case of hovering flapping flight are given by [4, 10]

$$Re = \frac{8\Phi R^2 f}{\nu \Lambda}, \quad K = \frac{\pi}{2\Phi \Lambda}. \quad (21)$$

where ν is the kinematic viscosity of the fluid medium, R is the wing length, Φ is the flapping amplitude, f is the flapping frequency in cycles/sec and Λ is the wing aspect ratio. Reduced frequency K is a measure of unsteadiness of the flow.

B. Robotic Flapper

In order to conduct experimental investigation, a robotic flapper was designed and fabricated at the University of Delaware. It is shown in Fig. 6. The flapper is driven by three independent servo motors designed to give three degrees-of-freedom flapping motion, i.e., ϕ , θ , ψ .

Flapper Kinematics

In our experiments, we keep the out of plane motion $\theta = 0$. This simplifies the kinematics but still retains the features of wing motion. The flapper coordinate system is shown in Fig. 7(A). For the case of hovering flight, the body of FWMAV is assumed to be stationary with respect to the earth. The body frame $f_o(\hat{x}_0, \hat{y}_0, \hat{z}_0)$ is also the inertial frame. The rotation matrices between the body frame and frame $f_1(\hat{x}_1, \hat{y}_1, \hat{z}_1)$ and between f_1 and wing frame $f_3(\hat{x}_3, \hat{y}_3, \hat{z}_3)$ are given by:

$$R_0^1 = \begin{pmatrix} C_\phi & 0 & S_\phi \\ S_\phi & 0 & -C_\phi \\ 0 & 1 & 0 \end{pmatrix}, \quad R_1^3 = \begin{pmatrix} 0 & 0 & 1 \\ C_\psi & -S_\psi & 0 \\ S_\psi & C_\psi & 0 \end{pmatrix} \quad (22)$$

The frame $f_4(\hat{x}_4, \hat{y}_4, \hat{z}_4)$ is the force/torque sensor frame. The F_x, F_y, F_z are the sensor read forces along

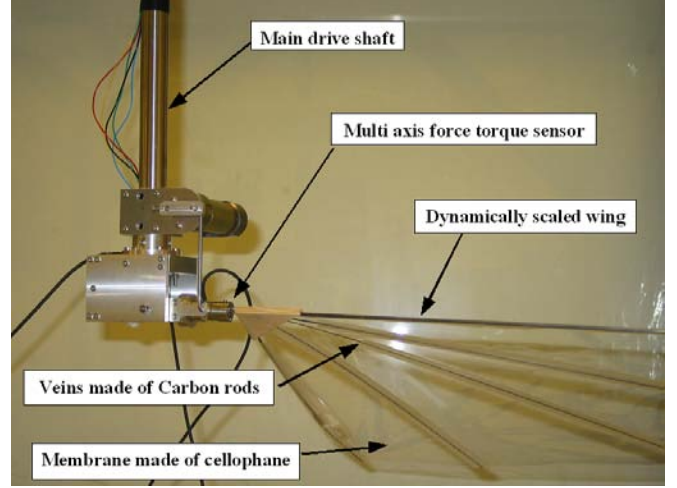


Fig. 6. Figure shows the robotic flapper designed and fabricated at University of Delaware. It is driven by three independent servo motors and can give 3-DOF flapping wing motion. A six-axis force torque sensor (Nano 17) from ATI industrial automation is mounted at the base of the wing. The aerodynamic forces and torques along with wing position can be seen real time with the help of this apparatus.

the directions $(\hat{x}_4, \hat{y}_4, \hat{z}_4)$ respectively. The rotation matrix between the wing frame f_3 and sensor frame f_4 is given by

$$R_3^4 = \begin{pmatrix} -1 & 0 & 0 \\ 0 & -1 & 0 \\ 0 & 0 & 1 \end{pmatrix}, \quad (23)$$

and

$$R_0^4 = R_0^1 R_1^3 R_3^4 = \begin{pmatrix} -S_\phi S_\psi & -S_\phi C_\psi & C_\phi \\ C_\phi S_\psi & C_\phi C_\psi & S_\phi \\ -C_\psi & S_\psi & 0 \end{pmatrix}. \quad (24)$$

The lift, drag force is given by

$$\begin{pmatrix} 0 \\ Lift \\ Drag \end{pmatrix} = R_1^4 \begin{pmatrix} F_x \\ F_y \\ F_z \end{pmatrix}, \quad (25)$$

where $Lift$ and $Drag$ are along \hat{y}_1 and \hat{z}_1 direction respectively. Similarly, the vertical and horizontal force is given by.

$$\begin{pmatrix} 0 \\ F_h \\ F_v \end{pmatrix} = R_0^4 \begin{pmatrix} F_x \\ F_y \\ F_z \end{pmatrix}. \quad (26)$$

where F_h is the horizontal force and F_v is the vertical force along the directions \hat{y}_o and \hat{z}_o respectively. Due to symmetry, we expect the force along the \hat{x}_o direction to

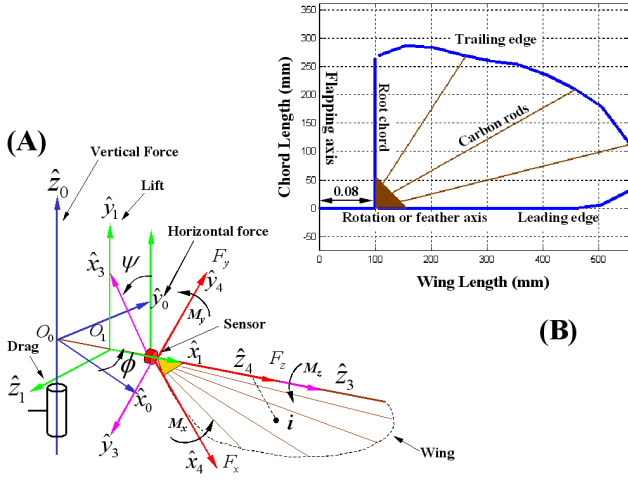


Fig. 7. (A) Figure shows the sensor co-ordinate frame f_4 and the positive direction of force and moment components ($F_x, F_y, F_z, M_x, M_y, M_z$). The direction of lift, drag, vertical and horizontal force are also identified. (B) Wing Planform used in the experiment.

cancel by the two opposite wings. The angular velocity of wing with respect to the earth frame is given by

$$\omega_{3/0} = \dot{\phi}\hat{z}_0 + \dot{\psi}\hat{z}_3. \quad (27)$$

Therefore, velocity of air at the point 'i' on the wing in frame f_4 is given by

$$\bar{u}(r, t) = -\dot{\phi}r \sin \psi \hat{x}_4 - (\dot{\phi}r \cos \psi + C_2 c(r) \dot{\psi}) \hat{y}_4 + C_2 c(r) \dot{\phi} \sin \psi \hat{z}_4. \quad (28)$$

For the estimation of total aerodynamic force given by Eq. (18), the velocity and normal acceleration components are required. For the robotic flapper, these are given by

$$|\bar{u}(r, t)|^2 = (\dot{\phi}r \sin \psi)^2 + (\dot{\phi}r \cos \psi + C_2 c(r) \dot{\psi})^2, \quad (29)$$

$$\dot{u}_n(r, t) = -(\ddot{\phi}r \cos \psi - \dot{\psi}\dot{\phi} \sin \psi + 0.5c(r) \ddot{\psi}), \quad (30)$$

where the velocity of air in the \hat{z}_4 direction is ignored because it is in the spanwise direction and does not contribute to the force. For estimation of \bar{a} , given by Eq. (5), the normal and tangential velocity components in the \hat{y}_4 and \hat{x}_4 directions respectively are given by

$$u_n(\hat{r}_2 R, t) = -(\dot{\phi}\hat{r}_2 R \cos \psi + C_2 \bar{c}\dot{\psi}), \quad (31)$$

$$u_t(\hat{r}_2 R, t) = -\dot{\phi}\hat{r}_2 R \sin \psi. \quad (32)$$

If we substitute $|\bar{u}(r, t)|^2$ and $\dot{u}_n(r, t)$ given by Eqs. (29) and (30) into Eq. (18), we get the total force as

$$F_T = C_1 F_1 + F_2(C_1, C_2) + C_3 F_3, \quad (33)$$

where

$$F_1 = \frac{\rho}{2} \dot{\phi}^2 \int_0^R r^2 c(r) dr \quad (34)$$

$$F_2 = \frac{\rho}{2} [2C_1 C_2 \dot{\phi} \dot{\psi} \cos \psi \int_0^R r c(r)^2 dr + C_2^2 \dot{\psi}^2 \int_0^R c(r)^3 dr] \quad (35)$$

$$F_3 = \frac{\rho\pi}{4} [-\ddot{\phi} \cos \psi \int_0^R r c(r)^2 dr + \dot{\psi} \dot{\phi} \sin \psi \int_0^R c(r)^2 dr - 0.5 \ddot{\psi} \int_0^R c(r)^3 dr] \quad (36)$$

where $C_1 F_1$ is the steady-state or LEV force, $C_3 F_3$ is the virtual mass force. The function F_2 captures the rotational force and it is an implicit function of the coefficients C_1 and C_2 . The integrals are a function of wing geometry.

C. Wing Design

Size and shape: The size of the wing can be determined from Eq. (21) based on Reynolds number. Reynolds number of hummingbird (*Lampornis clemenciae*) is 14,300 with a wing length of 85 mm, aspect ratio of 8.2, total stroke amplitude of 151 deg and a flapping frequency of 23.3 cycles/sec. A flapping wing MAV capable of hovering flight will be similar to a hummingbird in size and therefore the anticipated Re range for FWMAV design is between 12,000-25,000. Based on this Re range, we selected a generic insect-like wing shape for experiment shown in Fig. 7(B). It has the following scaled dimensions:

- Wing length $R = 0.58m$,
- Aspect ratio $\Lambda = 5.7677$,
- $\hat{r}_2 = 0.5628$ (dimensionless).
- Scaled flapping frequency = 0.5 cycles/sec

The wing geometry is given in Table I. Each element has constant width, i.e $dr = 0.05$ meters.

Wing fabrication

The wing structure is made of carbon rods representing the veins in a typical insect wing or feathers in hummingbird's wing. Carbon rods radiate from the triangular wing base made of balsa block. A cellophane membrane was attached to the structure using cellophane tape. The entire wing assembly weighs just 18 grams.

TABLE I
WING GEOMETRY USED IN THE EXPERIMENT

section	spanwise location 'r'(m),	chord c(r)(m),	$d_o(r)\%$
1	0.105	0.270	0
2	0.155	0.287	0
3	0.205	0.284	0
4	0.255	0.271	0
5	0.305	0.261	0
6	0.355	0.254	0
7	0.405	0.236	0
8	0.455	0.212	0
9	0.505	0.180	-0.12
10	0.555	0.115	-0.27

D. Measurement of Force and Moment

We used ATI Industrial Automation multi-axis force-torque sensor which can measure three forces F_x, F_y, F_z and three moment components M_x, M_y, M_z . The sensor can measure a maximum of ± 12 N in the F_x and F_y directions and ± 17 N in the F_z direction. The maximum moment range in all directions is ± 120 N-mm. The resolution for all three force components is $1/1280$ N and for all three moment components it is $1/256$ N-mm.

In order to reduce noise from the data, we used a simple low pass digital filter [14]. It is given by the following difference equation

$$y(n) = a y(n-1) + (1-a) x(n), \quad (37)$$

where $x(n)$ represents the discrete-time observed signal with $n = 0, 1, 2, \dots, N$ at the sample points. $y(n)$ is the smoothed output and $y(-1) = 0$. The parameter a is a weighting factor ($0 < a < 1$) selected between 0.7 and 0.8, depending on the noise in the data.

V. INITIAL OBSERVATIONS

The original force and torque data along with filtered data, in the sensor coordinate frame f_4 , for one particular kinematic pattern is shown in Fig. 8. This data includes the forces and moments due to gravity as well as inertia. In order to filter out the aerodynamic force, we used an identical wing but without the membrane (wing B). The wing with the membrane is referred to as wing A. The inertia and gravity loads from wing B were subtracted from wing A to get the aerodynamic force data.

Fig. 9 shows the aerodynamic and inertia loads from wing A, the inertia loads from wing B and the aerodynamic force in the sensor F_x, F_y and F_z directions for one stroke. A ten degree polynomial fit was done on the aerodynamic data to further smooth out the noise.

We know from revolving wing experiments [5], [6] that at high angles of attack (10° and up), the aerodynamic force is roughly normal to the wing surface and this was the assumption made in our aerodynamic model. This implies that the sensor should only detect the F_y component of force. However, initial results revealed the presence of F_x

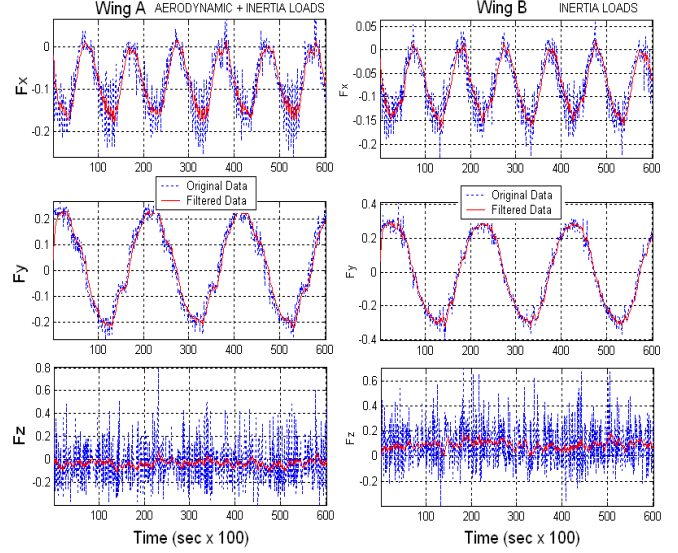


Fig. 8. Force Data in sensor frame f_4 of wing A and wing B (before and after filtering). The unit of force is 'N' (Newtons) and the unit of moment is 'N-mm'

and F_z components of the force besides the F_y component as shown in Fig. 8. From observations of the wing during the experiment, we concluded that the wing deforms due to the aerodynamic loads. Both spanwise bending and twist were present which are discussed separately below.

Spanwise Bending

Initially, the F_z data appeared simply as noise as shown in Fig. 8. However, after processing the data for one complete cycle, we observed that there was a definite aerodynamic force in the F_z direction. Fig. 9 shows the aerodynamic force F_z along the sensor \hat{z}_4 direction which is along the leading edge or feather axis of the wing (see Fig. 7(A)). If we examine the inertia loads from wing B, we see that there is a positive F_z force. This is most likely due to the centrifugal force trying to pull the wing out from the sensor. The results from wing A show a slight negative F_z force. We conclude that the possible explanation for the aerodynamic force in the negative F_z direction is wing bending as shown in Fig. 10(A). The aerodynamic force acts normal to every element of the wing and it is greatest close to the wing tip. The resultant aerodynamic force F_T bends the wing and creates a negative F_z component which seems to overcome the centrifugal force in this particular case. This can be further validated by the fact that the F_z component of aerodynamic force was found to be symmetric between the upstroke and downstroke.

Spanwise twist

Fig. 9 shows the aerodynamic force in the negative F_x direction. This was found during both the upstroke and the downstroke. The negative F_x force is most likely due to a twist along the wing length with the tip chord at an angle of roughly 10 to 20 degrees with respect to the root chord. As

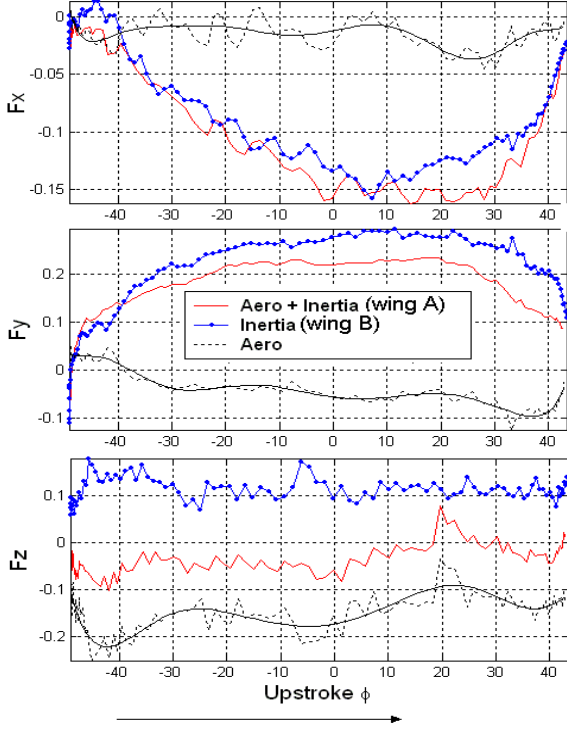


Fig. 9. Aerodynamic + inertia force of wing A, inertia force for wing B and filtered aerodynamic force for wing A during the upstroke. The unit of force is Newtons. A ten-degree polynomial fit is done on the aerodynamic data.

shown in Fig. 10(B), the i^{th} element of the wing undergoes twisting by an angle $\delta\psi_i$. The aerodynamic force dF_T^i still remains normal to the i^{th} element but it contributes a force in the negative F_x direction with respect to the sensor frame.

A. Modifications to the aerodynamic model

In order to better match the experimental results, the aerodynamic model should involve structural deflections to match with the physical wing. As a first approximation, we ignore the F_z component by assuming infinite rigidity in bending. We model twist by assuming a linear variation of twist from root to the tip of the wing. The twist $\delta\psi_i$ at the i^{th} section is given by

$$\delta\psi_i = \beta \frac{r_i - 0.08}{R - 0.08}, \quad (38)$$

where the unit of r_i and R is meters and 0.08 is the distance in meters between the root chord and the flapping axis and β is the magnitude of twist proportional to the aerodynamic moment about the feather axis. The inertial moment is ignored due to low flapping frequency of 0.5 Hz. The aerodynamic moment is assumed to be proportional to the normal velocity which is computed at a point located at a distance of $r = \hat{r}_2 R$ along the span from the flapping

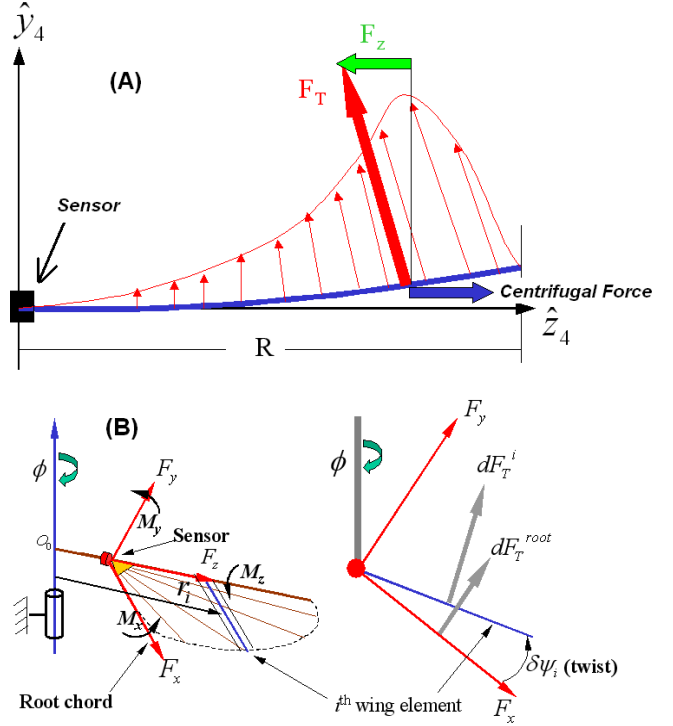


Fig. 10. (A) Shows how the spanwise bending creates a $-F_z$ component of the aerodynamic force which acts in $-\hat{z}_4$ direction in the sensor frame. The centrifugal force acts in the sensor $+\hat{z}_4$ direction. (B) shows how the spanwise twist $\delta\psi_i$ at the i^{th} element contributes to the $-F_x$ component of aerodynamic force in the sensor frame.

axis and at a distance of $C_2 \bar{c}$ along the chord from the feather axis. Therefore,

$$\beta = \pm K_\beta [u_n(\hat{r}_2 R, t)]^2. \quad (39)$$

The normal velocity is squared to give the same effect as aerodynamic force. Here, K_β is a coefficient to adjust the magnitude of β variation in a cycle due to normal velocity. In the current experiment the magnitude of the twist is visually matched with the experiment by varying the value of K_β . The \pm takes the sign of $u_n(\hat{r}_2 R, t)$ to give the correct direction of twist. The wing is considered rigid for computation of $u_n(\hat{r}_2 R, t)$.

Having an approximation of the aerodynamic twist, the total aerodynamic force is integrated vectorially from the root to the tip of the wing. Considering the i^{th} element of the wing located at a distance r_i from the flapping axis, the total force can be written as follows:

$$dF_T^i \cong C_1 \frac{\rho}{2} |\bar{u}(r_i, t)|^2 c(r_i) dr_i + C_3 \frac{\rho \pi}{4} \dot{u}_n(r_i, t) c(r_i)^2 dr_i. \quad (40)$$

Based on the assumption that the total force remains normal to the chord of any i^{th} element, we can transform this force

into the sensor frame as follows:

$$\begin{pmatrix} dF_x^i \\ dF_y^i \\ dF_z^i \end{pmatrix}_{\text{sensor}} = R_s^i \begin{pmatrix} 0 \\ dF_T^i \\ 0 \end{pmatrix}_{i^{th} \text{ element}}, \quad (41)$$

where R_s^i is the rotation matrix between each blade element and the sensor frame given as

$$R_s^i = \begin{pmatrix} C_{\delta\psi_i} & -S_{\delta\psi_i} & 0 \\ S_{\delta\psi_i} & C_{\delta\psi_i} & 0 \\ 0 & 0 & 1 \end{pmatrix}. \quad (42)$$

Here, $\delta\psi_i$ is the angle of twist of the i^{th} element with respect to the root chord. The moments in the sensor frame can be computed as follows:

$$dM_x^i = -r_i dF_y^i, \quad dM_y^i = r_i dF_x^i, \quad (43)$$

$$dM_z^i = [a - d_o(r_i)]c(r_i)dF_T^i, \quad (44)$$

where $d_o(r_i)$ is the non-dimensional distance between the rotation axis and the wing leading edge as shown in Fig. 5(A). The non-dimensional distance $a = 0.5$ gives the mid-chord location of dF_T^i at every section based on our assumption (see Section III. E).

The forces and moments can be summed in the sensor frame in order to get the total force and moment components

$$F_x = \sum_{i=1}^N dF_x^i, \quad F_y = \sum_{i=1}^N dF_y^i, \quad F_z = \sum_{i=1}^N dF_z^i = 0 \quad (45)$$

$$M_x = \sum_{i=1}^N dM_x^i, \quad M_y = \sum_{i=1}^N dM_y^i, \quad M_z = \sum_{i=1}^N dM_z^i \quad (46)$$

Since the F_z component of sensor force is ignored, the resultant force F_T in the sensor frame can be written as

$$F_T = \sqrt{F_x^2 + F_y^2}. \quad (47)$$

The inclusion of moderate spanwise twist will have insignificant effect on the magnitude of C_1 [5]. We further assume that it has no effect on coefficients C_2 and C_3 . Therefore, based on this assumption, the sensor output, F_T could still be used to find the coefficients using Eq. (33) for rigid wing by ignoring the twist and Eq. (40) and Eq. (45) can then be used to determine the force components by taking into account the twist. In the computation of kinematics and angle of attack, the twist $\delta\psi_i$ is ignored.

VI. DETERMINATION OF COEFFICIENTS

The sensor measures the total aerodynamic force F_T given by Eq. (47). The functions F_1 , F_2 and F_3 in Eq. (33) capture the physics of the particular unsteady effect and the coefficients simply adjust the magnitude. Once the magnitudes of C_1 , C_2 and C_3 are adjusted at any point during the flapping cycle, these functions are expected to be robust enough to match the experimental data throughout cycle. We determined the coefficients as follows.

A. Determination of C_1

In order to determine C_1 , we select the flapping kinematics such that the functions F_2 and F_3 become zero at some point in the flapping cycle but F_1 remains non-zero. This means $\dot{\phi} \neq 0$, while $\dot{\psi} = \ddot{\phi} = \ddot{\psi} = 0$. The following simple kinematic pattern was selected using Eqs. (1)-(3).

$$\phi(t) = \Phi \sin(\omega t) \quad , \quad \phi_o = \zeta_{\phi_n} = 0, \quad n = 1 \quad (48)$$

$$\theta(t) = 0 \quad , \quad \theta_o = \Theta_n = 0 \quad (49)$$

$$\psi(t) = -\Psi \cos(\omega t) \quad , \quad \psi_o = 0, \quad \zeta_{\psi_n} = \frac{\pi}{2}, \quad n = 1 \quad (50)$$

This pattern gives maximum values of $\dot{\phi}$ and $\ddot{\psi}$ at the mid-stroke position where $\dot{\psi} = 0$. The term involving $\ddot{\psi}$ in F_3 gives the rotational virtual mass effect which is small in comparison to the translational virtual mass effect and therefore we ignore it in subsequent analysis. In other words, F_2 and F_3 both become close to zero and only the translational force, $F_{lev} = C_1 F_1$ is non-zero at the mid-stroke. Therefore, the sensor measures $F_T = F_{lev}$ and

$$C_1 = \frac{F_T}{F_1} = \frac{F_{lev}}{1/2\rho \dot{\phi}^2 \int_0^R r^2 c(r) dr}, \quad \text{at } \phi = 0, \quad (51)$$

where F_T is determined from force sensor components F_x and F_y . The integral $\int_0^R r^2 c(r) dr$ turns out to be simply one half of the second moment of area S_2 [3]. This gives a simple form for the determination of C_1 , i.e.,

$$C_1 = \frac{F_{lev}}{1/4 \rho \dot{\phi}^2 S_2}. \quad (52)$$

Procedure

For the safe operation of robotic flapper, the flapping frequency was limited to 0.5 Hz. This together with the wing geometric parameters, gives the Reynolds number Re and reduced frequency K as a function of flap amplitude

$$Re = \frac{15450\pi}{180} \times \Phi \quad , \quad K = \frac{0.2725 \times 180}{\pi} \frac{1}{\Phi}. \quad (53)$$

TABLE II
TESTING SCHEME

Flap Amplitude Φ (deg).	Re	K
46	12,404	0.332
63	17,000	0.2477
74.5	20,000	0.2095

TABLE III
ANGLE OF ATTACK AT MID-STROKE, ($\phi = 0^0$)

s.no.	Rotational Amplitude Ψ (deg).	$\bar{\alpha}$ (deg)
*	90.0	0.0
1	75.0	15.0
2	64.0	26.0
3	52.4	37.6
4	41.2	48.8
5	30.0	60.0
6	19.0	71.0
7	8.0	82.0
8	0.0	90.0

Three different values of flap amplitude Φ were chosen (46, 63, and 74.5 degrees) as shown in Table II. Each flap amplitude gives a different value of Reynolds number Re and reduced frequency K . This conforms with different flap amplitudes of flapping used by biological species.

For each flap amplitude, the rotational amplitude Ψ and eight corresponding $\bar{\alpha}$ from 0 to 90 degrees were chosen at the mid-stroke position, as shown in Table III. In fact, $\bar{\alpha}$ varies between -90 and 90 degrees during the cycle, giving two values of force at the same $\bar{\alpha}$, differing only in sign. We averaged the two forces and determined an average C_1 corresponding to $\bar{\alpha}$ at the mid-stroke position. We did not conduct the experiment at $\bar{\alpha} = 0$ deg and assumed $C_1(0) = 0$. This is because normal force is zero on a symmetric flat plate at zero angle of attack. The chordwise friction force is ignored in our model. In all, 24 kinematic patterns were tested.

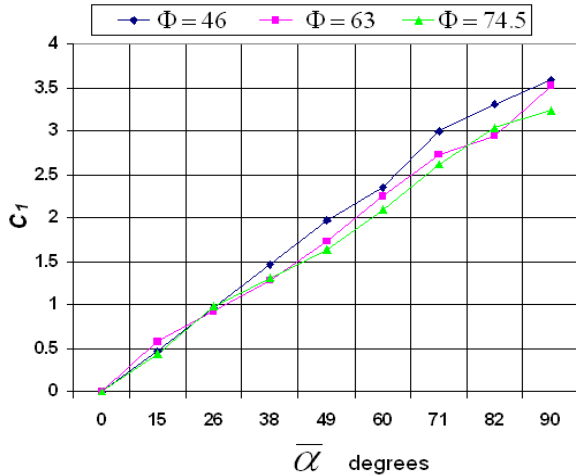


Fig. 11. Coefficient of LEV/translational force C_1 Vs $\bar{\alpha}$

The plot of C_1 against $\bar{\alpha}$ is shown in Fig. 11 for the three different stroke amplitudes. This shows that the coefficient of translational force varies linearly with $\bar{\alpha}$. Furthermore, the flap amplitude and consequently Re has little effect on the slope ($dC_1/d\alpha$). From Fig 11, we can approximate C_1 as linearly varying with $\bar{\alpha}$ given by

$$C_1(\bar{\alpha}) = \frac{7}{\pi} \bar{\alpha}, \quad (54)$$

where $\bar{\alpha}$ is in radians.

B. Determination of C_2

C_1 and C_2 occur implicitly in F_2 . Therefore, the best way to determine C_2 is to adjust it until the model matches with the experimental results. Furthermore, $C_2 = d_i - d_o(r)$ varies along the span. $d_o(r)$ is known from the wing geometry and given in Table I. The value of C_2 is based on d_i . We found that $d_i = 0.75$ gives best results. In computing F_2 , the coefficient C_1 is considered a known parameter. Therefore, C_1 is determined before C_2 .

C. Determination of C_3

If we modify the kinematic pattern given by Eqs. (48)-(50) by taking $\Psi = 0^0$ in Eq. (50), then F_2 becomes zero for the entire cycle while F_1 becomes zero at the ends of the stroke, i.e., at $\phi = \phi_{max}$ and $\dot{\phi} = 0$. However, F_3 is maximum there since $\ddot{\phi}$ is maximum. Therefore, the total force, F_T , measured by the sensor at the ends of the stroke is due to virtual mass effect.

$$C_3 = \frac{F_T}{F_3} = \frac{F_{virtual\ mass}}{F_3}, \quad \text{at } \phi = \phi_{max}. \quad (55)$$

The value of C_3 was found to vary between 0.5 and 1.0 for all 24 kinematic patterns.

VII. COMPARISON OF EXPERIMENTAL RESULTS

Most of the published data on flapping wings is for flapping translational motion of the wing, i.e; without rotation. The only way to compare it with our experimental data is to compare it at the mid-stroke of flapping cycle where wing rotation becomes zero instantaneously, for all the kinematic patterns given by Eq. (48-50). Secondly, the published data is in the form of either coefficients of lift and drag or coefficients of vertical and horizontal force. Therefore, in order to compare our experimental data, we determined the coefficients of lift and drag at the mid-stroke position using the lift and drag forces.

A. Lift, drag, vertical and horizontal force

The aerodynamic force components (F_x, F_y, F_z) which correspond to ($\hat{x}_4, \hat{y}_4, \hat{z}_4$) directions in the sensor frame f_4 , were transformed into lift, drag, vertical and horizontal components for the entire cycle using Eqs. (25) and (26).

As shown in Fig. 12, the lift and vertical components are positive for both the upstroke and downstroke while

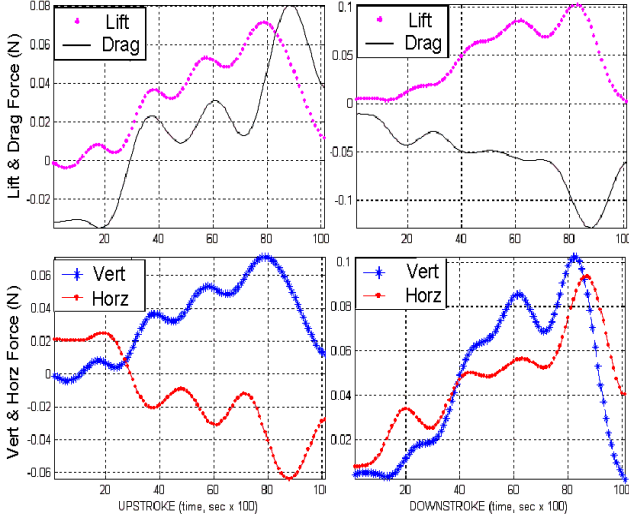


Fig. 12. **Lift, Drag, horizontal and vertical force components for $\Phi = 46^\circ$ and $\Psi = 52.4^\circ$ in the sensor frame f_4**

the drag and vertical force components cancel out during the cycle. This is expected since the kinematic pattern given by Eq. (48-50) is symmetric between the upstroke and downstroke. Therefore, a net vertical force is generated corresponding to a hovering flight. A net horizontal and drag component is produced if the kinematic pattern is not symmetric.

B. Coefficients of lift and drag force

The coefficient of lift and drag are computed from the lift and drag force plots at the mid-stroke position using Eq. (52).

$$C_L = \frac{Lift}{1/4 \rho \phi^2 S_2}, \quad C_D = \frac{Drag}{1/4 \rho \phi^2 S_2} \quad (56)$$

Eq. (52) is applicable since C_L and C_D are the decomposition of C_1 . The polar plot of C_L and C_D for the three flap amplitudes ($\Phi = 46, 63, 74.5$ deg) is shown in Fig. 13. The polar plot shows high values of C_L and C_D compared to linearly translating wings [5] and compares well with the published data Sane [11], Usherwood and Ellington [5], [6]. The only major difference can be seen at the maximum value of C_D in Fig. 13 where the plot does not go to zero. This is because we tested a wing which could also twist under the aerodynamic loads. Therefore, at the maximum angle of attack, i.e., 90° when the coefficient of drag is maximum (close to 3.5), we get added lift due to spanwise twist. The polar plot also show that the coefficients do not vary with flapping amplitudes. However, for a given flapping frequency, large stroke amplitudes generate greater lift due to the fact that the wings sweep a larger area with higher translational velocity. Therefore, we conclude that large stroke amplitude is vital for generating higher vertical force during hovering flight.

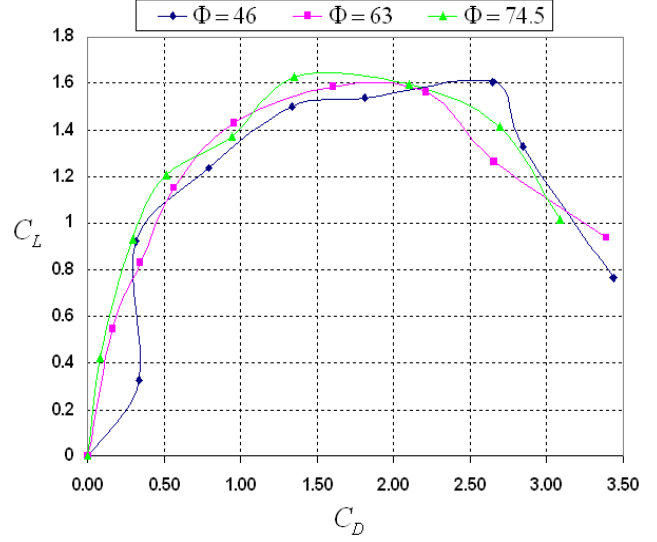


Fig. 13. **Lift and drag polar plot for three stroke amplitudes, i.e., $\Phi = 46^\circ, 63^\circ, 74.5^\circ$. These coefficients are computed at the mid-stroke position during the flapping cycle similar to the determination of C_1**

VIII. COMPARISON OF EXPERIMENTAL RESULTS WITH AERODYNAMIC MODEL

The coefficients C_1 , C_2 and C_3 will now be used in the aerodynamic model and comparison will be made with the experimental data. Note that C_1 and C_3 were computed from the experimental data but C_2 was tuned to fit the experimental results. In order to compare the aerodynamic model with the experiment, we will compare two kinematic patterns. From Table III, we select two patterns having rotational amplitude of $\Psi = 75^\circ$ and $\Psi = 0^\circ$ (entries 1 and 8 in Table III). In both cases, the flap amplitude is $\Phi = 46^\circ$. These represent the extreme cases. The experiment was not conducted at $\Psi = 90^\circ$. If the model compares well with the experimental data for these two extreme cases, we will have more confidence that the comparison will be good for the patterns in between. The kinematic patterns for these two cases are shown in Fig. 14, where arrows indicate instantaneous direction of motion.

A. Comparison of kinematics

In Fig. 15, we compare the flap angle ϕ and rotational angle ψ with the experimental data from the encoder. The kinematic pattern is given by Eq. (48)-(50). The complete cycle takes 2 seconds at flapping frequency of 0.5 cycles/sec. Note that the maximum value of $\psi = \Psi$ occurs at the mid-stroke (at time = 50 and 150 milliseconds) with a corresponding minimum angle of attack during the entire cycle. The comparison of ϕ and ψ is good throughout the cycle.

B. Comparison of twist $\delta\psi$

Fig. 15 also shows the variation of twist $\delta\psi$ at the tip section during the cycle modeled by Eqs. (38) and (39).

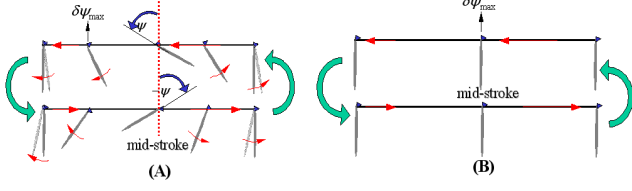


Fig. 14. (A) This kinematic pattern has flapping and rotational amplitudes of $\Phi = 46^\circ$ and $\Psi = 74.9^\circ$ respectively. The arrows indicates instantaneous direction of motion of a wing section. At mid-stroke, $\psi = 0$, the section is undergoing flapping translation. (B) This kinematic pattern has flapping and rotational amplitudes of $\Phi = 46^\circ$ and $\Psi = 0^\circ$ respectively. Section is undergoing translational motion only. Figure also shows roughly the location of maximum twist $\delta\psi_{max}$ as observed during the experiment.

The model predicts maximum twist $\delta\psi_{max}$ at the mid-stroke position (time = 50, 150 milliseconds) for pattern (B). This location is also shown in Fig. 14(B). For pattern (A), $\delta\psi_{max}$ occurs when the wing passes through the mid-stroke position and roughly close to the end of the stroke as shown in Fig. 15. This location is roughly shown in Fig 14(A). This is because $\delta\psi$ is directly proportional to the normal velocity according to Eq. (38) and (39) which turns out to be the greatest when the wing undergoes both rotational and translational motion near the end of the stroke. Note that Eq. (38) and (39) give an approximate representation of the actual wing twist. The amplitude of twist was matched visually with the physical wing through trial and error by varying K_β . During the actual experiment, we did notice the pattern of $\delta\psi$ at the wing tip similar to Fig. 15 with the maximum twist occurring near the end of the stroke for pattern (A) and at the mid-stroke position for pattern (B).

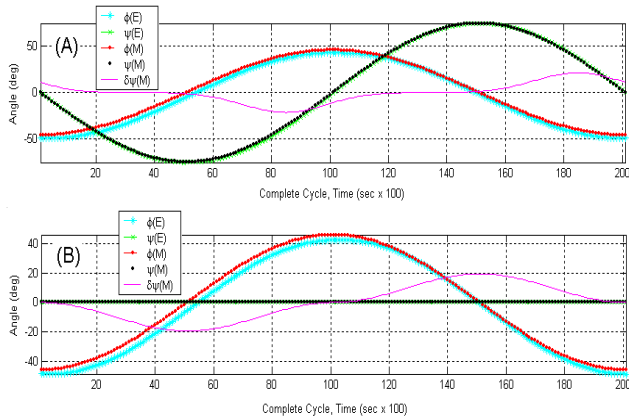


Fig. 15. Comparison of kinematic patterns, (E)=Experiment, (M)= Model. Pattern (A) $\Phi = 46^\circ$, $\Psi = 74.9^\circ$ and Pattern (B) $\Phi = 46^\circ$, $\Psi = 0^\circ$ show a good match with the model. Plot also shows the twist $\delta\psi$ at the tip section computed using Eqs. (38) and (39)

C. Comparison of F_y component of aerodynamic force

Fig. 16 shows the F_y component of aerodynamic force in the sensor frame for the two kinematic patterns. Plots (A) and (B) show the force data for the patterns having flapping and rotational amplitudes of $\Phi = 46^\circ$ and $\Psi = 74.9^\circ$ while (C) and (D) represent the pattern having amplitudes of $\Phi = 46^\circ$ and $\Psi = 0^\circ$. The F_y component was computed using Eq. (45). Figs 16(A) and (C) are the plots of individual aerodynamic mechanisms (C_1F_1 , F_2 , C_3F_3) which are components of the total force transformed in the sensor F_y direction for half cycle. Figs 16(B) and (D) shows how the individual aerodynamic mechanisms contribute to the total force and match very well with the experimental results.

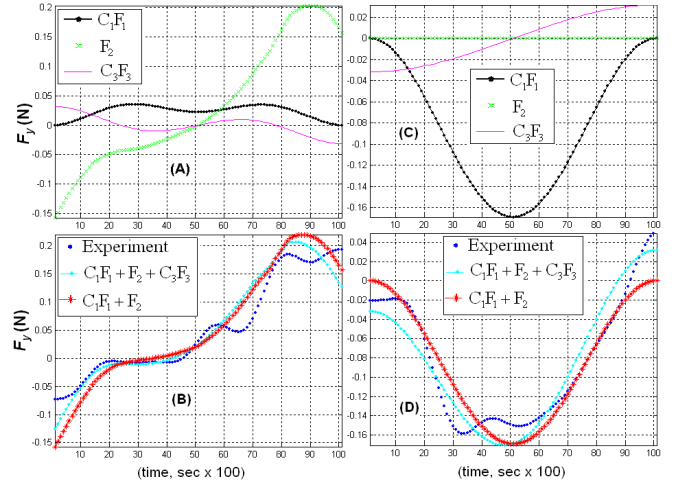


Fig. 16. Comparison of F_y component of total aerodynamic force $F_T = C_1F_1 + F_2(C_1, C_2) + C_3F_3$. (A) and (B) shows the comparison for the pattern having amplitudes $\Phi = 46^\circ$, $\Psi = 74.9^\circ$, (C) and (D) shows the comparison for the pattern having amplitudes $\Phi = 46^\circ$, $\Psi = 0^\circ$.

For the patterns in Figs 16(A) and (B), the rotational force F_2 dominates as far as magnitude is concerned. This shows that the quasi-steady aerodynamic force given by C_1F_1 , is inadequate for modeling flapping wing aerodynamics when the rotation is present. Furthermore rotational and virtual mass force F_2 and C_3F_3 respectively are seen to be zero at the mid-stroke position while the translational force C_1F_1 is zero at the ends. This is because the functions F_2 and F_3 are zero while F_1 is not zero at the mid-stroke ($\phi = 0^\circ$).

For the pattern shown in (C) and (D), the rotational force is zero throughout the cycle since $\psi = 0$ and the wing undergoes flapping translation only. Therefore, we see that the translational force C_1F_1 dominates throughout the cycle except at the ends of the stroke where it is zero. The virtual mass force C_3F_3 is maximum at the ends of the stroke and adjusts the total force at the ends as shown in Fig. 16(D). This kinematic pattern was specially selected to study the virtual mass effect since this is the only effect present at the ends of the stroke.

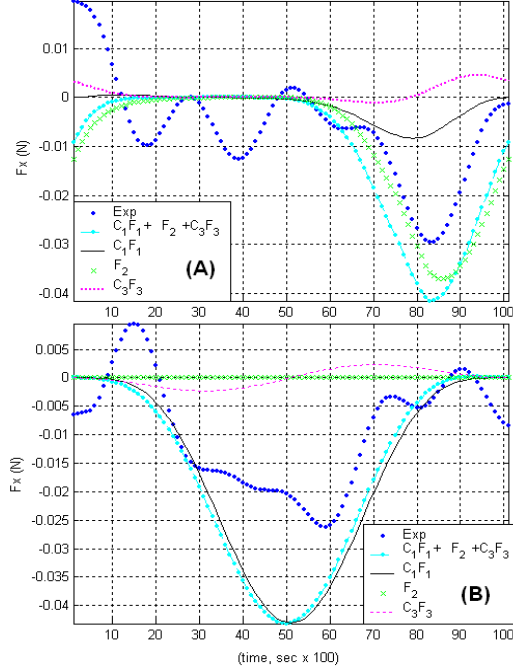


Fig. 17. Comparison of F_x component of total aerodynamic force F_T . (A) shows the comparison for the pattern having amplitudes $\Phi = 46^\circ$, $\Psi = 74.9^\circ$, (B) shows the comparison for the pattern having amplitudes $\Phi = 46^\circ$, $\Psi = 0^\circ$

D. Comparison of F_x component of aerodynamic force

The F_x component of aerodynamic force is computed using Eq. (45) and compared with the experimental data as shown in Fig. 17 for the two kinematic patterns. The match with the experimental data is less accurate in the case of F_x component. This is probably due to the approximate match of twist $\delta\psi$ with the actual wing in terms of both the spanwise distribution as well as variation during the cycle. The model assumes linear twist from the root to the tip of the wing. The actual twist distribution could be different. It should be noted that the approximation of twist does not affect the F_y component because its magnitude is more than three times that of the F_x component and the error is not visible in the F_y plot. We found this typical behavior in all the 24 kinematic patterns.

E. Comparison of aerodynamic moments

The sensor measures the aerodynamic moments as well as the aerodynamic force. Therefore, we can compare the experimentally obtained moments with the moments computed from the aerodynamic model. In Fig. 18, the three plots in column (A) and (B) show the three components of moments (M_x , M_y , M_z) belonging to the two selected kinematic patterns.

The moments are computed using Eq. (46). The M_x and M_z components show a good match with the experimental data. The accuracy of M_x component indicates that the model accurately distributes the F_y component along the

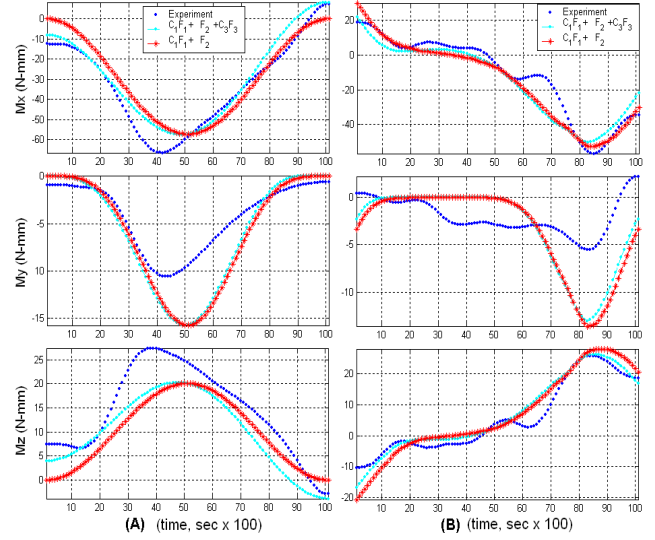


Fig. 18. Comparison of moments (M_x , M_y , M_z). These are computed based on the assumption that the aerodynamic force at each section dF_T acts at the mid-chord location. (A) shows the results for the kinematic pattern having amplitudes $\Phi = 46^\circ$, $\Psi = 74.9^\circ$, and (B) shows the results for the kinematic pattern having amplitudes $\Phi = 46^\circ$, $\Psi = 0^\circ$.

span. The magnitude of F_y has already been verified from comparison of the force plots. Similarly, the accuracy of M_z component indicates that our assumption of mid-chord location of force dF_T at every section given by the parameter ' $a = 0.5$ ' in Eq. (44) is valid. The comparison of M_y component is approximate due to the fact that it is dependent on F_x component of force which compared approximately with the experiment as discussed earlier. This behavior of moments was found to be consistent in all 24 kinematic patterns.

F. Comparison of the location of resultant aerodynamic force

The location of the resultant aerodynamic force on the wing for one stroke is also compared with the experiment and shown in Fig. 19. The distance \bar{a} (chord-wise direction) and the distance \bar{b} (spanwise direction) give the location of the resultant aerodynamic force. This is another way to test our assumption that the total force dF_T at every section acts at the mid-chord location, i.e., $a = 0.5$. \bar{a} and \bar{b} were calculated using the values of force and moment at the location of force/torque sensor for both the model and experiment using the following equations.

$$\bar{a} = \frac{M_z}{F_y} \quad , \quad \bar{b} = \frac{-M_x}{F_y}. \quad (57)$$

Fig. 19 shows good comparison of aerodynamic and experimental values of force location (\bar{a} and \bar{b}) for one kinematic pattern. Fig. 19 also indicates that the location of force does not vary during the stroke except near the very ends.

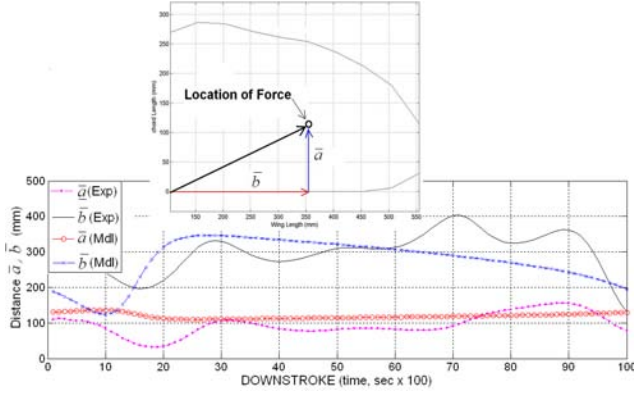


Fig. 19. Location of resultant aerodynamic force on the wing given by the distance \bar{a} and \bar{b} for the kinematic pattern ($\Phi = 46^\circ$ and $\Psi = 64^\circ$). Note ‘Exp’ stands for experimental and ‘Mdl’ stands for aerodynamic model.)

IX. CONCLUSION

This paper presents a methodology for the experimental determination of unsteady aerodynamic force coefficients based on the principle of dynamic similarity. These coefficients are used in the quasi-unsteady aerodynamic model which additionally takes into account the wing twist due to aerodynamic loads. The key conclusions drawn from this work are given below

- 1) We found a good match of F_y , F_z , M_x and M_z components and an approximate match of F_x and M_y components of resultant force and moment at the base of the wing for all the 24 kinematic patterns.
- 2) The coefficient of translational force C_1 is determined as a function of angle of attack at one point during the flap cycle. Similarly, the coefficient C_2 and C_3 are determined as constants for the entire flapping cycle. However, the model matches the experimental data for the entire cycle and for all kinematic patterns. This indicates that the functions F_1 , F_2 and F_3 are robust and capture the trend or physics of the unsteady effects.
- 3) The variation of stroke amplitude Φ at constant flapping frequency does not alter the translational force coefficient C_1 . However, an increase in stroke amplitude results in higher lift and drag forces during the cycle. This means that high stroke amplitude is essential for hovering flight.
- 4) The model assumes that for high angles of attack, typically encountered in hovering flapping flight, the total aerodynamic force remains normal to the chord and the chordwise component is zero for the entire cycle. The good match of model and experimental results indicates that the total force remains roughly normal to the chord for the entire cycle as assumed. In making this conclusion, we have taken into account the approximate spanwise twist in the model.

- 5) We also found that the effects of virtual mass force are small compared to translational and rotational effects at the Re range of 12,000 to 20,000. In our model, we have assumed that $C_3 F_3$ is virtual mass effect. However, it might be wake capture effect because both act in a similar manner. This needs to be verified using PIV measurements.
- 6) Moderate spanwise twist has very little effect on the magnitude of C_1 and total force F_T , however, it changes the force components in the sensor frame significantly. This implies significant change in the direction of resultant force vector. For wings with large spanwise twist, the procedure should be modified by decomposing C_1 into horizontal C_h and Vertical C_v coefficient of force. However, we have not pursued this method.

REFERENCES

- [1] DELaurier, J. D., “An Aerodynamic Model for Flapping-Wing Flight”. *Aeronautical Journal*, Vol. 97, No. 964 April 1993, pp.125-130.
- [2] Hao Liu, Ellington, C. P. Kawachi Keiji, Van Den Berg and Willmott A.P.; “A Computational Fluid Dynamic Study of Hawkmoth Hovering”. *Journal of Experimental Biology*, 201, 461-477 (1998).
- [3] Ellington, C. P. (1984a). “The aerodynamics of hovering insect flight. I-V”. *Phil. Trans. Royal Society of London B* 305, 115.
- [4] Ellington, C. P. (1999). “The novel aerodynamics of insect flight: applications to micro-air vehicles.”. *J. Exp. Biol.* 202, 34393448.
- [5] Usherwood, J. R. and Ellington, C. P. (2002). “The aerodynamics of revolving wings. I”. *J. Exp. Biol.* 205, 15471564.
- [6] Usherwood, J. R. and Ellington, C. P. (2002). “The aerodynamics of revolving wings. II”. *J. Exp. Biol.* 205, 15471564.
- [7] Willmott A. P., Ellington, C. P. and Adrian L.R. Thomas (1997). “Flow visualization and unsteady aerodynamics in the flight of the hawkmoth, *Manduca sexta*.” *Phil. Trans. R. Soc. Lond. B* (1997) 352, 303-316.
- [8] Van Den Berg, and Ellington, C. P. (1997). “The three dimensional leading-edge vortex of a hovering model hawkmoth.” *Phil. Trans. R. Soc. Lond. B* 352, 329340.
- [9] Dickinson, M.H, Lehmann, F.O., Sane, S.P (1997). “Wing Rotation and the Aerodynamic Basis of Insect Flight.”
- [10] Azuma, A, Okamoto, M and Yasuda, K “Aerodynamic Characteristics of Wings at low Reynolds number”.
- [11] Sane, S.P (2003). “The aerodynamics of insect flight” *Journal of Experimental Biology*, 206, 4191-4208 (2003)
- [12] Sane, S.P, and Dickinson, M.H (2001). “The aerodynamic effects of wing rotation and a revised quasi-steady model of flapping flight” *Journal of Experimental Biology*, 205, 1087-1096 (2002)
- [13] Walker, J. A., (2002). “Rotational lift: something different or more of the same?”. *Journal of Experimental Biology*, 205, 3783-3792 (2002).
- [14] Advanced Engineering Mathematics 2nd ed by Harman, Dabney and Richert.
- [15] Robert Dudley. “The biomechanics of insect flight, form, function and evolution.”
- [16] Sun, M. and Tang, J. (2002). Unsteady aerodynamic force generation by model fruit fly wing in flapping motion. *J. Exp. Biol.* 205, 55-70.
- [17] Sanjay P.Sane and Michael H. Dickinson (2001). “The control of flight force by a Flapping Wing: Lift and Drag Production” accepted 18th May 2001